 CMES, vol.88, no.6, pp.475-506, 2012

Asymmetric Shell Elements Based on a Corrected Updated-Lagrangian Approach

P. Areias[1,2,3], T. Rabczuk[4] and D. Dias-da-Costa[5,6]

Abstract: Surprisingly good displacement results are obtained by using the Petrov-Galerkin method with assumed and enhanced metric components in the test functions and enhanced metric components in the trial functions. Cartesian trial functions are required to ensure completeness and assumed/enhanced metric components are introduced to ensure high coarse-mesh accuracy. In the trial functions, the original incompatible-mode in-plane Q6 element by Wilson *et al.* can be used without violating the patch test. As a beneficial side-effect, Newton-Raphson convergence behavior for non-linear problems is improved. Transverse-shear and in-plane patch tests are satisfied while distorted-mesh performance is better than with symmetric formulations due to the absence of coordinate transformation. Covariant coordinates are used to calculate the (mixed) test metric and a combination of Cartesian coordinates and quadratic terms in the metric are used for the trial functions. Classical test functions with assumed metric components are required for compatibility reasons. Verification tests are performed with very good performance being observed in all of them. Applications to large displacement elasticity and finite strain plasticity are shown with both low sensitivity to mesh distortion and high accuracy. A equilibrium-consistent (and consistently linearized) updated-Lagrangian algorithm is proposed and tested. Concerning the time-step dependency, it was found that the consistent updated-Lagrangian algorithm is nearly time-step independent and can replace the multiplicative plasticity approach if only moderate elastic strains are present.

[1] Corresponding Author. ISI search: areias p*; email: pmaa@uevora.pt, pareias@civil.ist.utl.pt, Ph.: +351 96 3496307, Fax: +351 266745394, URL: http://evunix.uevora.pt/~pmaa/

[2] Physics Department, University of Évora, Colégio Luís António Verney, Rua Romão Ramalho, 59, 7002-554 Évora, Portugal

[3] ICIST

[4] Institute of Structural Mechanics, Bauhaus-University Weimar, Marienstraße 15, 99423 Weimar, Germany

[5] INESC Coimbra, Rua Antero de Quental 199, 3000-033 Coimbra

[6] Civil Eng. Dept., University of Coimbra, Rua Luís Reis Santos, 3030-788 Coimbra, Portugal

1 Introduction

Finely discretized geometries in ductile damage and precise crack propagation simulations (cf. Areias, Garção, Pires, and Infante Barbosa (2011); Rabczuk and Areias (2006); Rabczuk, Areias, and Belytschko (2007)) require, as a condition for efficient solution and robustness, sound algorithms and thorough testing and assessment. For shells, this verification process includes a set of obstacle problems beginning with the patch tests (in-plane, bending and transverse shear), classical beam, plate and shell benchmarks and including large displacement and finite strain tests. Assessing elements with finite displacement tests and finite strain plasticity tests is also important as these have been found to uncover certain instabilities (see, e.g. Crisfield and Peng (1996)) with unconventional formulations. Element technology for low-order quadrilateral shells is too vast to be summarized in this manuscript and most elements proposed in the last decades vary only slightly in performance for the same number of degrees-of-freedom. A milestone in the removal of out-of-plane locking problem (i.e. the transverse shear locking) was set with the assumed natural strain technique Dvorkin and Bathe (1984); Park and Stanley (1986) and in-plane bending locking was removed in 1973 by the celebrated Wilson Q6 element Wilson, Taylor, Doherty, and Ghaboussi (1973) and subsequent corrections. For undistorted meshes, convergence rate of the results is established regardless of the incomplete higher order terms in the polynomials (see the treatise Belytschko, Liu, and Moran (2000)) and these higher order terms only contribute to stability and coarse-mesh accuracy. Of course, mesh distortion adversely affects the convergence rate and it has been a problem without the same definite solution that the shear locking problem benefited from. An exception has been the remarkable work of Rajendran and co-workers Rajendran and Liew (2003); Ooi, Rajendran, and Yeo (2004) who proposed the use of the Petrov-Galerkin projection for elasticity with high degree of mesh distortion performance. Cartesian coordinates are used for the trial functions and parent-domain coordinates for the test functions. They applied this approach to elasticity with quadratic elements balancing high performance in the two element test *and* satisfaction of the patch test. However, two important topics were not studied:

1. The combination with incompatible modes and assumed natural strains, necessary for low order elements.

2. The application to geometrically non-linear problems and finite strain plasticity problems.

In addition to these two topics, several other aspects are discussed and tested in this work. A serious obstacle in applying the work of Rajendran and co-workers

to finite strains is that, being the trial shape functions dependent on the spatial coordinates, the linearization costs would be predictably high and some robustness concerns appeared at an earlier attempt of using the classical spatial formulation (as in the seminal work of J. Simo Simo (1992); Simo and Armero (1992)) and $\boldsymbol{F}_e\boldsymbol{F}_p$ plasticity. It became clear that an alternative, less cumbersome, technique would allow the extension of these works to include both locking remedies and non-linear terms. We therefore describe the technique in the following four sections. After this, a sequence of both linear and non-linear *well-known* benchmark tests is performed with a high degree of accuracy and mesh distortion insensitivity. Finally, conclusions are drawn in section 7.

2 Governing equations

2.1 Static equilibrium for an arbitrary reference configuration

Cauchy equations of equilibrium for any reference configuration can be obtained from the corresponding spatial equilibrium (the derivations for the latter are shown in Ogden Ogden (1997) and extended here). Using standard notation (cf. Truesdell and Noll (2004)) we write the spatial version of Cauchy equations as (j is the facet index):

$$\frac{\partial \sigma_{ij}}{\partial x_{p_j}} + b_i = 0 \tag{1}$$

with σ_{ij} $(i,j = 1,2,3)$ being the components of the Cauchy stress in an orthonormed basis and b_i the components of the body force vector. The coordinates x_{p_j} are the spatial, or deformed, coordinates of a given point (p) under consideration. It is implied that (1) is satisfied for a time parameter $t \in [0,T]$ with T being the total time of analysis and for a position $\boldsymbol{x}_p \in \Omega_t$ belonging to the deformed position domain at the time of analysis (here denoted Ω_t). In tensor notation, the equation (1) can be presented as:

$$\nabla \cdot \boldsymbol{\sigma}^T + \boldsymbol{b} = \boldsymbol{0} \tag{2}$$

where $\nabla = \frac{\partial}{\partial \boldsymbol{x}_p}$ is the spatial gradient operator. To complement (2), essential and natural boundary conditions defined in terms of two functions g_i and h_i are required (cf. Hughes (2000)):

$$u_i = g_i \quad \text{on} \quad \Gamma_{g_i} \tag{3}$$

$$\sigma_{ij} n_j = h_i \quad \text{on} \quad \Gamma_{h_i} \tag{4}$$

where the boundary $\Gamma_t = \partial\Omega_t$ is partitioned in $\Gamma_{\boldsymbol{g}}$ and $\Gamma_{\boldsymbol{h}}$: $\Gamma_t = \Gamma_{\boldsymbol{g}} \cup \Gamma_{\boldsymbol{h}}$ (the essential and the natural boundaries). In equation (4), n_j are the components of outer

normal to Γ_t (in the deformed configuration). Using the definition of the first Piola-Kirchhoff tensor ($\boldsymbol{P}$) and denoting the deformation gradient as $\boldsymbol{F}$, it is possible to modify the derivatives in (1). Making use of the relation $\boldsymbol{\sigma} = \frac{1}{J}\boldsymbol{P}\boldsymbol{F}^T$ with $J = \det \boldsymbol{F}$ we can write the equilibrium equation in material form as:

$$\frac{\partial P_{ij}}{\partial X_{p_j}} + Jb_i = 0 \tag{5}$$

where X_{p_j} are the material, or undeformed, coordinates of a given point under consideration. A direct manipulation of (5) with the use of the second Piola-Kirchhoff stress, $\boldsymbol{S}$, allows the writing the alternative material form of equilibrium:

$$F_{ik}\frac{\partial S_{kj}}{\partial X_{p_j}} + Jb_i = 0 \tag{6}$$

or, using ∇_0 as the material gradient operator (the derivative with respect to $\boldsymbol{X}_p$):

$$\boldsymbol{F}\nabla_0 \cdot \boldsymbol{S}^T + J\boldsymbol{b} = \boldsymbol{0} \tag{7}$$

The time parameter t is, in equation (7), the same as it was in equation (2). However, the position domain is now $\Omega_0 \equiv \Omega_t|_{t=0}$. At this point, given (6), the conclusion of arbitrariness of X_{p_j} as reference coordinates allows us to use a reference configuration corresponding to an arbitrary instant t_b and the associated position domain Ω_b. Note that there is no requirement concerning this configuration, i.e. t_b is not necessarily in $[0,T]$. This results in the following generalization of (7):

$$\boldsymbol{F}_b\nabla_b \cdot \boldsymbol{S}_b^T + J_b\boldsymbol{b} = \boldsymbol{0} \tag{8}$$

where

$$\nabla_b = \frac{\partial}{\partial \boldsymbol{X}_{pb}} \tag{9}$$

$$\boldsymbol{F}_b = \nabla_b \boldsymbol{x} \tag{10}$$

$$J_b = \det \boldsymbol{F}_b \tag{11}$$

$$\boldsymbol{S}_b = J_b \boldsymbol{F}_b^{-1}\boldsymbol{\sigma}\boldsymbol{F}_b^{-T} \tag{12}$$

The time parameter t is, in equation (8), the same as it was in equation (2) and the position domain is now $\Omega_b \equiv \Omega_t|_{t=t_b}$. The reader can now observe that, if a given time instance t_a is chosen from the interval $[0,T]$ not necessarily coinciding with t, we can re-write (8) as:

$$\boldsymbol{F}_{ab}\nabla_b \cdot \boldsymbol{S}_{ab}^T + J_{ab}\boldsymbol{b} = \boldsymbol{0} \tag{13}$$

with $\boldsymbol{F}_{ab} = \nabla_b \boldsymbol{x}_{pa}$, $\boldsymbol{S}_{ab}^T = \boldsymbol{S}_{ab}$ etc. This conclusion will be used in the weak form of equilibrium. The reader can note that it is possible to transform the boundary conditions (3-4) to the material setting. However, if boundary finite elements are used, they can be directly written in the deformed configuration.

A fact worth pointing out is the following: t_a must be an equilibrium instant, in contrast with t_b. This explains why simplification attempts of the equilibrium equation (8) by switching $\boldsymbol{F}_{ab}$ for $\boldsymbol{I}$[1] result in loss of convergence for high values of deformation.

2.2 Kinematics and stress integration

If (13) is adopted as the equilibrium equation with time parameters t_a and t_b, stress integration can be used in a form that avoids the polar decomposition or (explicit) objective rates. In a previous work Areias and Belytschko (2006) a rate-independent rotational approach is proposed, but it entails a more complex constitutive algorithm in finite strains. The present derivation can be used to achieve an efficient and robust time-integration scheme for finite plastic strains. In addition, if $t_b = 0$, hyperelastic models can be used directly in the material form (as discussed at length in Holzapfel (2000)). Let us consider three configurations a, b and c (respectively at times $t_a \geq t_b \geq t_c$) as depicted in Figure 1. A consistent (and consistently linearized) updated-Lagrangian formulation is derived from (13) and the stepping suggested in that Figure. The formulation can also be viewed as total Lagrangian, since the strain-displacement matrices are similar in structure to the ones for this formulation.

The relative deformation gradient between two configurations Ω_a and Ω_b is given by[2]:

$$\boldsymbol{F}_{ab} = \frac{\partial \boldsymbol{x}_{pa}}{\partial \boldsymbol{x}_{pb}} \tag{14}$$

or, using the covariant basis (cf. Areias, Ritto-Corrêa, and Martins (2010)), the following product is obtained:

$$\boldsymbol{F}_{ab} = \boldsymbol{x}_a^T \boldsymbol{y}_b \tag{15}$$

where

$$\boldsymbol{x}_a = \left(\frac{\partial \boldsymbol{x}_{pa}}{\partial \boldsymbol{\theta}} \right)^T \tag{16}$$

[1] Those modifications result in sparse strain-displacement operators coinciding with the small strain case, in contrast with what is presented here.

[2] Scalar components of $\boldsymbol{F}_{ab}$ are introduced as $[\boldsymbol{F}_{ab}]_{ij}$ for the i^{th} row and j^{th} column.

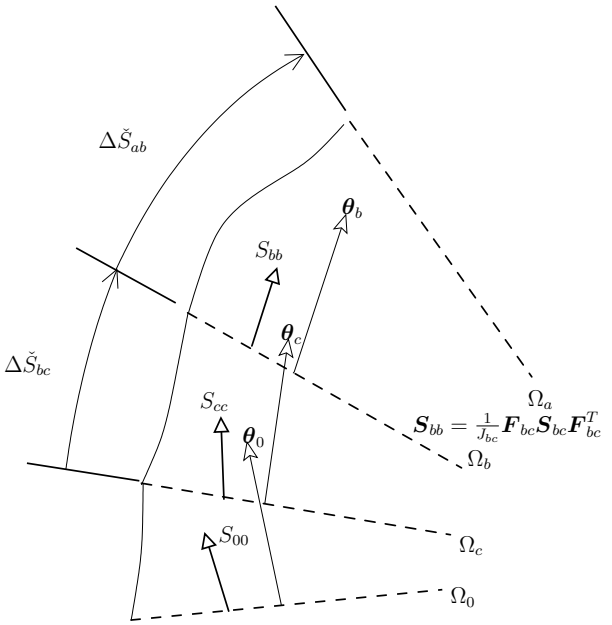

Figure 1: Intermediate configurations used for stress integration. $\boldsymbol{\theta}$ denote curvilinear coordinates, $\boldsymbol{\theta} = \{\theta^1, \theta^2, \theta^3\}$.

contains, as rows, the covariant basis vectors of configuration a. Curvilinear coordinates $\boldsymbol{\theta}$ are often locally identified with the parent domain coordinates, but need not be. In addition, $\boldsymbol{y}_a = \boldsymbol{x}_a^{-T}$ contains, as columns, the contravariant basis vectors of the same configuration. The inverse of the deformation gradient is obtained by swapping indices a and b: $\boldsymbol{F}_{ab}^{-1} = \boldsymbol{F}_{ba}$. The Jacobian determinant, using the same notation, is given by:

$$J_{ab} = \det \boldsymbol{F}_{ab} \tag{17}$$

and measures the ratio between the volumes at configurations a and b. The spatial covariant metric is defined as:

$$\boldsymbol{m}_{aa} = \boldsymbol{x}_a \boldsymbol{x}_a^T \tag{18}$$

The spatial velocity gradient is given from the derivative of $\boldsymbol{x}_a$: $\boldsymbol{l}_{ab} = \dot{\boldsymbol{x}}_a^T \boldsymbol{y}_b$ and the strain rate as its symmetric part: $\dot{\boldsymbol{\varepsilon}}_{ab} = \frac{1}{2}\boldsymbol{y}_b^T \dot{\boldsymbol{m}}_{aa} \boldsymbol{y}_b$. Of course, using the spatial metric we can write the right Cauchy-Green tensor (see Ogden (1997) for the nomenclature) between two configurations a and b directly obtained from its definition (15) as:

$$\boldsymbol{C}_{ab} = \boldsymbol{y}_b^T \boldsymbol{m}_{aa} \boldsymbol{y}_b \tag{19}$$

Stress tensors are also naturally given in relation to two configurations a and b. Specifically, using the Cauchy stress tensor ($\boldsymbol{S}_{aa}$ or $\boldsymbol{\sigma}$ in the classical notation) can be obtained from the second Piola-Kirchhoff stress $\boldsymbol{S}_{ab}$ between a and b[3]:

$$\boldsymbol{S}_{aa} = \frac{1}{J_{ab}} \boldsymbol{F}_{ab} \boldsymbol{S}_{ab} \boldsymbol{F}_{ab}^T \tag{20}$$

The reference configuration for the stress can be changed from b to c by a direct generalization of (20):

$$\boldsymbol{S}_{ac} = \frac{J_{ac}}{J_{ab}} \boldsymbol{F}_{cb} \boldsymbol{S}_{ab} \boldsymbol{F}_{cb}^T \tag{21}$$

Obviously, power-conjugate quantities involving this definition of stress must be of the form:

$$\dot{w} = \frac{1}{2} \boldsymbol{S}_{ab} : \dot{\boldsymbol{C}}_{ab} \tag{22}$$

$\forall t_a > t_b$. The weak form of equilibrium is given by (the upper triangle indicates a "virtual quantity", as employed by S.S. Antman Antman (2005)):

$$\underbrace{\frac{1}{2} \int_{\Omega_b} \boldsymbol{S}_{ab} : \overset{\triangle}{\boldsymbol{C}}_{ab} \mathrm{d}\Omega_b}_{\overset{\triangle}{W}_{\mathrm{int}}} = \overset{\triangle}{W}_{\mathrm{ext}} \tag{23}$$

when $t_a > t_b$ and, alternatively,

$$\int_{\Omega_a} \boldsymbol{S}_{aa} : \overset{\triangle}{\boldsymbol{\varepsilon}}_{aa} \mathrm{d}\Omega_a = \overset{\triangle}{W}_{\mathrm{ext}} \tag{24}$$

when $t_a = t_b$. These two forms follow directly from (2) and (13) in the previous section and the application of Green's theorem. The so-called "stress updates" in the sense of approximations for the Lie derivative (see Chapters 7 and 8 of Simo and Hughes (2000)) are typically given as:

$$\boldsymbol{S}_{ab} = \Delta \check{\boldsymbol{S}}_{ab} + \underbrace{\frac{1}{J_{bc}} \boldsymbol{F}_{bc} \boldsymbol{S}_{bc} \boldsymbol{F}_{bc}^T}_{\boldsymbol{S}_{bb}} \tag{25}$$

with $\Delta \check{\boldsymbol{S}}_{ab}$ being the relative constitutive stress[4] and $\boldsymbol{S}_{bb}$ can be interpreted as the "transported" stress, whose source is purely kinematic, as Figure 1 suggests. The

[3] As discussed before, $\boldsymbol{S}_{ab}$ can be interpreted as the second Piola-Kirchhoff stress at time t_a relative to the reference configuration at time t_b

[4] Both elastic and inelastic parts contribute to $\Delta \check{\boldsymbol{S}}_{ab}$

strict total Lagrangian formulation is recovered for $b = c = 0$. When considering plasticity it is convenient for $\Delta\check{\boldsymbol{S}}_{ab}$ to depend on a "strain" measure, which in our case is the relative Green-Lagrange strain:

$$\boldsymbol{E}_{ab} = \frac{1}{2}\left[\boldsymbol{C}_{ab} + \boldsymbol{I}\left(2\alpha T_{ab} - 1\right)\right] \tag{26}$$

where α is the linear thermal expansion coefficient and T_{ab} is the temperature difference between configurations a and b. For completeness, we also show that the back-stresses (here denoted by $\boldsymbol{B}$) are given by a similar update scheme,

$$\boldsymbol{B}_{ab} = \Delta\check{\boldsymbol{B}}_{ab} + \underbrace{\frac{1}{J_{bc}}\boldsymbol{F}_{bc}\boldsymbol{B}_{bc}\boldsymbol{F}_{bc}^{T}}_{\boldsymbol{B}_{bb}} \tag{27}$$

To create a stress contour map, of course Cauchy stresses are physically meaningful and correspond to $\boldsymbol{S}_{aa}$, calculated as $\boldsymbol{S}_{aa} = \boldsymbol{F}_{ab}\left(\Delta\check{\boldsymbol{S}}_{ab} + \boldsymbol{S}_{bb}\right)\boldsymbol{F}_{ab}^{T}/J_{ab}$ with the appropriate transformations for a global coordinate system. The proposed approach implies a re-writing of classical $\boldsymbol{F}_e\boldsymbol{F}_p$ plasticity codes to work with time increments (one of such codes is discussed in Areias and Rabczuk (2010)). The linearization of (23) is straightforward (with fewer operations at the constitutive level than the traditional Kirchhoff-stress/strain rate approach) and follows:

$$\overset{\triangle}{\mathrm{d}W}_{\mathrm{int}} = \frac{1}{2}\int_{\Omega_b}\boldsymbol{S}_{ab} : \mathrm{d}\overset{\triangle}{\boldsymbol{C}}_{ab}\mathrm{d}\Omega_b + \frac{1}{4}\int_{\Omega_b}\mathrm{d}\boldsymbol{C}_{ab} : \mathscr{C} : \overset{\triangle}{\boldsymbol{C}}_{ab}\mathrm{d}\Omega_b \tag{28}$$

and $\mathrm{d}W_{\mathrm{ext}}$ being calculated according to the deformation-dependent loads. The determination of $\boldsymbol{C}_{ab}$ and $\boldsymbol{F}_{ab}$ does not have to be compatible in the sense that since an updated problem is solved when switching from b to c as reference configuration, it follows that mixed formulations can be used for $\boldsymbol{C}_{ab}$ and not for $\boldsymbol{F}_{bc}$ in (25). Restrictions to moderate *elastic* strains are of course applicable once b and c do not coincide. The interesting versatility of the present approach is that for hyperelastic materials we can coalesce $b = c = 0$ and the Lagrangian description of hyperelasticity can be used *without* specific conditions and for arbitrarily large strains. Otherwise, it is clear that a Lie derivative of the stress is being implicitly calculated and the proposed algorithm belongs to the non-corotational hypoelastic class of algorithms (discussed in Bruhns, Meyers, and Xiao (2004)). The following limitations are known to exist with this approach:

- Energy dissipation for large amplitude closed loading cycles.
- Restriction to elastic isotropy when using elasto-plastic constitutive laws.

In contrast with the $\boldsymbol{F}_e\boldsymbol{F}_p$ approaches, where errors result from the plastic integration algorithm (cf. Areias, Dias-da Costa, Pires, and Infante Barbosa (2011)), in the present approach the stress time integration has an associated error without plastic flow. A direct comparison with classical approximations (Kirchhoff/Saint-Venant using the Hencky strain) and hyperelastic models (Neo-Hookean according to the description by Wriggers Wriggers (2008)) is made to assess the range of elastic deformations for which the present approach can be accepted (cf. Figure 2). When considering elasticity, high values of step size result in stress drifting. It is noticeable that, for metal elasto-plasticity, the error is not important since elastic strain components are typically less than 1%.

3 Position vector in a shell, metric and related derivations

Equation (19) is fundamental for the assumed-metric approach in the test functions. Shells further constrain that metric, as described by the classical work of Antman and Marlow Antman and Marlow (1991), resulting in a specific form of the position vector. For a shell, it is known that a possible $\boldsymbol{x}_{pa} \in \Omega_a$ is[5] the following:

$$\boldsymbol{x}_{pa} = \boldsymbol{r}_{pa} + \frac{h_a \theta^3}{2} \boldsymbol{d}_{pa} \tag{29}$$

where $\boldsymbol{r}_{pa}$ is the mid-surface position vector in Ω_a, θ^3 is a non-dimensional, thickness-like coordinate, h_a is the thickness at position $\boldsymbol{r}_{pa}$ and, finally, $\boldsymbol{d}_{pa}$ is a unit director. This nomenclature is standard and is adopted in Areias, Ritto-Corrêa, and Martins (2010). We choose to avoid drilling degrees-of-freedom and therefore two rotation parameters are sufficient to describe the motion of the directors. The director's relation to the rotation parameters is:

$$\boldsymbol{d}_{pa} = \boldsymbol{\Gamma}_0 \boldsymbol{Q}(\alpha_1, \alpha_2) \begin{Bmatrix} 0 \\ 0 \\ 1 \end{Bmatrix} \tag{30}$$

where $\boldsymbol{\Gamma}_0$ is the fiber coordinate system transformation matrix (the method described by Hughes Hughes (2000) and Hughes and Liu Hughes and Liu (1981) is adopted). The rotation matrix $\boldsymbol{Q}(\alpha_1, \alpha_2)$ and its derivatives are determined using the software Wolfram Mathematica Research Inc (2007) with the add-on AceGen Korelc (2002). In a shorter notation, (30) can be written as:

$$\boldsymbol{d}_{pa} = \boldsymbol{\Gamma}_0 \begin{Bmatrix} \frac{\sin\alpha}{\alpha}\alpha_2 \\ -\frac{\sin\alpha}{\alpha}\alpha_1 \\ \cos\alpha \end{Bmatrix} \tag{31}$$

[5] We omit the similar case of b

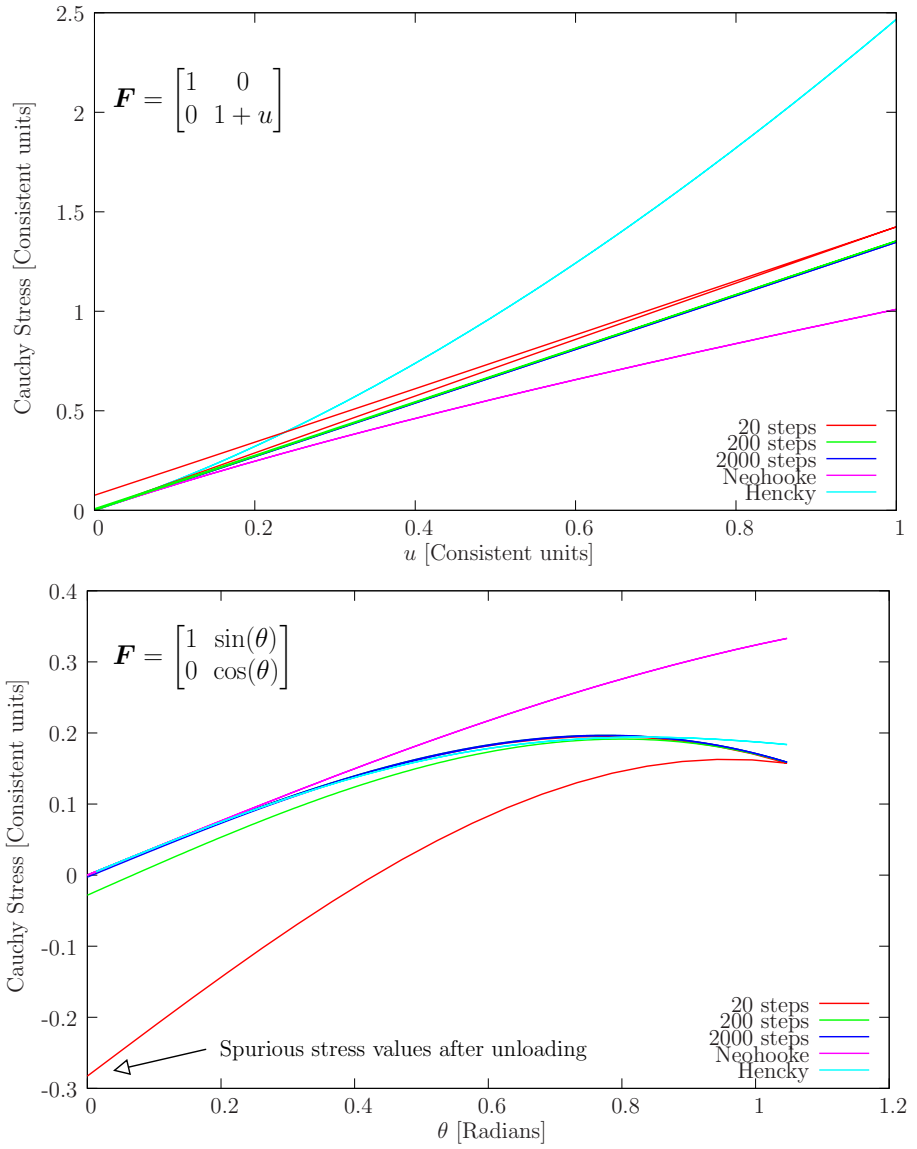

Figure 2: Closed loading cycle with high values of *elastic* strains: comparison with Neo-Hookean and Kirchhoff/Saint-Venant using the Hencky strain.

with $\alpha = \sqrt{\alpha_1^2 + \alpha_2^2}$. The property $\boldsymbol{d}_{pa} \cdot \frac{\partial \boldsymbol{d}_{pa}}{\partial \theta^i} = 0$ for $i = 1,2$ produces the following metric components:

$$[\boldsymbol{m}_{aa}]_{ij} = \boldsymbol{r}_{pa_i} \cdot \boldsymbol{r}_{pa_j} + \frac{h_a \theta^3}{2} \left[\left(\boldsymbol{r}_{pa_i} \cdot \boldsymbol{d}_{pa_j} + \boldsymbol{r}_{pa_j} \cdot \boldsymbol{d}_{pa_i} \right) + \frac{h_a \theta^3}{2} \boldsymbol{d}_{pa_i} \cdot \boldsymbol{d}_{pa_j} \right] \tag{32}$$

$$[\boldsymbol{m}_{aa}]_{i3} = \frac{\kappa_s h_a}{2} \boldsymbol{r}_{pa_i} \cdot \boldsymbol{d}_{pa} \tag{33}$$

$$[\boldsymbol{m}_{aa}]_{33} = \frac{h_a^2}{4} \tag{34}$$

with $i = 1,2$ and $j = 1,2$. In (32), we consider $\boldsymbol{r}_{pa_i}$ as the derivative of $\boldsymbol{r}_{pa}$ with respect to θ^i. Finally, κ_s is the shear correction parameter, usually taken as $5/6$, which scales the shear terms so that the correct energy is obtained. Another aspect that deserves attention is the singularity problem in (31) Brank and Ibrahimbegovic (2001). We propose a method to deal with this: rotations are always relative to the Kirchhoff director[6], as depicted in Figure 3. Metric components are all calculated from $\boldsymbol{r}_p$ and $\boldsymbol{d}_p$ from the internal products of (32).

4 Asymmetric interpolations

4.1 Test functions

We adopt the traditional shape function interpolation for $\boldsymbol{r}_{pa}$ and $\boldsymbol{d}_{pa}$:

$$\boldsymbol{r}_{pa} = \boldsymbol{n}_r(\boldsymbol{\theta}) \boldsymbol{r}_{aN} \tag{35}$$

$$\boldsymbol{d}_{pa} = \boldsymbol{n}_r(\boldsymbol{\theta}) \boldsymbol{d}_{aN} \tag{36}$$

with $\boldsymbol{r}_{aN}$ and $\boldsymbol{d}_{aN}$ being the nodal mid-surface positions and the nodal directors, respectively. The directors $\boldsymbol{d}_{aN}$ are calculated using the angles $\Delta\alpha_1$ and $\Delta\alpha_2$ using the expressions by Hughes Hughes (2000). The shape function matrix for the $4-$node quadrilateral, $\boldsymbol{n}_r$, is given as:

$$\boldsymbol{n}_r = \frac{1}{4} \begin{bmatrix} \cdots & \left(1+\theta^{1K}\theta^1\right)\left(1+\theta^{2K}\theta^2\right) & 0 & 0 & 0 & \cdots \\ \cdots & 0 & \left(1+\theta^{1K}\theta^1\right)\left(1+\theta^{2K}\theta^2\right) & 0 & 0 & \cdots \\ \cdots & 0 & 0 & \left(1+\theta^{1K}\theta^1\right)\left(1+\theta^{2K}\theta^2\right) & \left(1+\theta^{1K}\theta^1\right)\left(1+\theta^{2K}\theta^2\right) & \cdots \end{bmatrix} \tag{37}$$

[6] In the time-step algorithm we use the converged Kirchhoff director at $t = t_b$ so that essential boundary conditions for the rotation can still be applied.

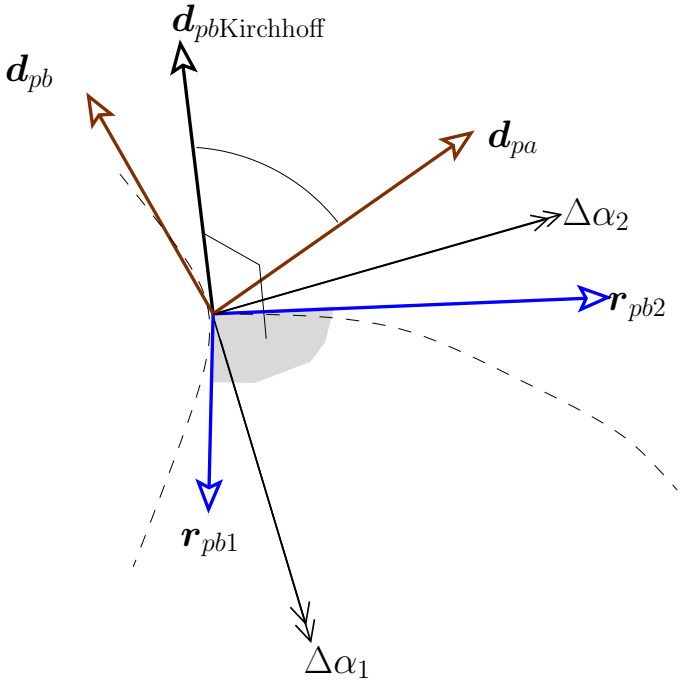

Figure 3: Rotations relative to the Kirchhoff director at $t = t_b$.

with θ^{iK} represent the curvilinear coordinates evaluated at each node K. The right Cauchy-Green tensor for the test functions is given by the following equation, which is obtained by using assumed and enhanced metric (see also Areias, César de Sá, Conceição António, and Fernandes (2003)) :

$$\begin{aligned} \boldsymbol{C}_{ab}^{\text{test}} \;=\; & \boldsymbol{y}_b^T \begin{bmatrix} m_{11} & m_{12} & 0 \\ m_{21} & m_{21} & 0 \\ 0 & 0 & m_{33} \end{bmatrix} \boldsymbol{y}_b + \\ & \bar{\boldsymbol{y}}_b^T \begin{bmatrix} 0 & 0 & N_A m_{13A} + N_B m_{13B} \\ 0 & 0 & N_C m_{23C} + N_D m_{23D} \\ N_A m_{13A} + N_B m_{13B} & N_C m_{23C} + N_D m_{23D} & 0 \end{bmatrix} \bar{\boldsymbol{y}}_b + \\ & \frac{\sqrt{\det[\bar{\boldsymbol{m}}_{bb}]}}{\sqrt{\det[\boldsymbol{m}_{bb}]}} \bar{\boldsymbol{y}}_b^T \begin{bmatrix} \theta^1\gamma_1 & \theta^1\gamma_3 + \theta^2\gamma_4 & 0 \\ \theta^1\gamma_3 + \theta^2\gamma_4 & \theta^2\gamma_2 & 0 \\ 0 & 0 & 0 \end{bmatrix} \bar{\boldsymbol{y}}_b \end{aligned} \tag{38}$$

where the components m_{ij} with $i = 1,2,3$ and $j = 1,2,3$ correspond to the components $[\boldsymbol{m}_{aa}]_{ij}$. The subscripts A, B, C and D indicate the points with the corresponding parent-domain coordinates and the terms N_A, N_B, N_C and N_D indicate the following shape functions, as described in Table 1. In (38), $\bar{\boldsymbol{y}}_b$ are evaluated at the element center point ($\boldsymbol{\theta} = \boldsymbol{0}$) so that the Patch test is satisfied. Along the same lines (cf. Simo and Armero (1992) for a similar approach), the enhanced metric term makes use of the metric at the element center $\overline{\boldsymbol{m}}_{bb}$. The parameters γ_l,with$l = 1,\ldots,4$ in (38) are additional degrees-of-freedom, condensed out at the element level.

Table 1: Functions used in the assumed metric technique

I	N_I	$\boldsymbol{\theta}_I$
A	$\frac{1}{4}(2-\theta^1)$	$\{-1,0,0\}$
B	$\frac{1}{4}(2+\theta^1)$	$\{1,0,0\}$
C	$\frac{1}{4}(2-\theta^2)$	$\{0,-1,0\}$
D	$\frac{1}{4}(2+\theta^2)$	$\{0,1,0\}$

The test function $\overset{\triangle}{\boldsymbol{C}}_{ab}$ is obtained from $\boldsymbol{C}_{ab}^{\text{test}}$ given in (38) as:

$$\overset{\triangle}{\boldsymbol{C}}_{ab} = \frac{\partial \boldsymbol{C}_{ab}^{\text{test}}}{\partial \boldsymbol{r}_{aN}} \overset{\triangle}{\boldsymbol{r}}_{aN} + \frac{\partial \boldsymbol{C}_{ab}^{\text{test}}}{\partial \boldsymbol{d}_{aN}} \overset{\triangle}{\boldsymbol{d}}_{aN} \tag{39}$$

where $\overset{\triangle}{\boldsymbol{r}}_{aN}$ and $\overset{\triangle}{\boldsymbol{d}}_{aN}$ are test functions for the nodal mid-surface position and director, respectively. Contrary to the trial functions, the first derivative of $\overset{\triangle}{\boldsymbol{C}}_{ab}$ is needed to obtain the linearized form (28).

4.2 Trial functions

The test right Cauchy-Green tensor $\overset{\triangle}{\boldsymbol{C}}_{ab}$ is here obtained using different shape functions than those employed for $\boldsymbol{C}_{ab}$. In particular, we use interpolation in Cartesian coordinates x,y,z[7] (at $t = t_b$) for $\boldsymbol{C}_{ab}$ and the classical parent-domain interpolation for $\overset{\triangle}{\boldsymbol{C}}_{ab}$ (θ^1, θ^2 and θ^3). We use the classical Vandermonde matrix and corresponding interpolation for an arbitrarily function $\phi(\boldsymbol{x}_b)$:

$$\phi(\boldsymbol{x}_{pb}) = p_i(\boldsymbol{x}_{pb}) \left[p_i(\boldsymbol{x}_{pbJ})\right]^{-1} \phi_J \tag{40}$$

[7] Where the following notation is used $x_1 = x$, $x_2 = y$, $x_3 = z$.

where $\boldsymbol{x}_{pbJ}$ corresponds to J^{th} node position at $t = t_b$. In (40) summation in indices i and J is implied. The polynomial basis $\boldsymbol{p}$ is classically given by the following column-vector:

$$\boldsymbol{p} = \{1, x, y, z, xy, xz, yz, xyz\}^T \tag{41}$$

Eight parameters are required for the interpolation and for this we construct a fictitious hexahedron to obtain the 8×8 coefficients in (40) by extruding, along an averaged normal, the quadrilateral contained in the reference plane. After this is performed, shape functions and corresponding derivatives are obtained directly in terms of $\boldsymbol{x}_{pb}$:

$$\boldsymbol{x}_{pa} = M_J(\boldsymbol{x}_{pb})\boldsymbol{x}_{paJ} \tag{42}$$

where summation in J is implied. The term $\boldsymbol{x}_{paJ}$ in (42) corresponds to the nodal positions at $t = t_a$. In terms of costs, we only compute the inverse $\left[p_i\left(\boldsymbol{x}_{pbJ}\right)\right]^{-1}$ at each element once, and this is a 8×8 inverse with a total cost of around 8^3 multiplications and divisions only using the cubic cost and *without* accounting for pivoting, which depends on the numerical coefficients.

The deformation gradient is obtained taking the derivative of (42) when $\phi = \boldsymbol{x}_{pa}$. We then have, in terms of components,

$$[\boldsymbol{F}_{ab}]_{kl} = \frac{\partial [\boldsymbol{x}_{pa}]_k}{\partial \left[\boldsymbol{x}_{\text{pb}}\right]_l} = \frac{\partial p_i}{\partial \left[\boldsymbol{x}_{pb}\right]_l} \left[p_i\left(\boldsymbol{x}_{pb_J}\right)\right]^{-1} [\boldsymbol{x}_{pa_J}]_k \tag{43}$$

Classically, the right Cauchy-Green tensor is simply given by:

$$\boldsymbol{C}_{ab} = \boldsymbol{F}_{ab}^T \boldsymbol{F}_{ab} \tag{44}$$

The introduction of enhanced metric components in the test functions requires the same to be performed in the trial functions and therefore we include the same terms here (cf. Areias, César de Sá, Conceição António, and Fernandes (2003)):

$$\boldsymbol{C}_{ab}^{\text{trial}} = \boldsymbol{F}_{ab}^T \boldsymbol{F}_{ab} + \boldsymbol{y}_b^T \left[\sum_{J=1}^{N_J} \boldsymbol{M}_J(\boldsymbol{\theta})\gamma_J\right] \boldsymbol{y}_b \tag{45}$$

with γ_J being additional degrees-of-freedom, as mentioned before. Four internal degrees-of-freedom are adopted corresponding to the in-plane bending modes. Note that, in contrast with the requirements for the test functions, there is no need to use a constant $\boldsymbol{y}_b$ and scale the Jacobian for the trial functions. It actually corresponds to the original Q6 element by Wilson *et al.* Wilson, Taylor, Doherty, and Ghaboussi (1973). It is well known that this further improves the performance for

distorted meshes. The original Q6 element does not satisfy the plane patch tests, while the present element does since compatible test functions are adopted. Finally, there is no need to use assumed metric components in the trial functions, since transverse shear is properly accounted for.

5 Multiple-surface plasticity for *moderate* elastic strains

Constraints shown in Figure 2 limit the applicability of plasticity formulations to moderate elastic strains. As shown in that Figure, around up to 10 in elastic strain can be safely used without spurious stresses in unloading.

Recently, we have proposed a general integration algorithm for large plastic strains with multiple yield functions in Areias, Dias-da Costa, Pires, and Infante Barbosa (2011). Kinematic hardening and plastic anisotropy were considered in that paper, but for the present work we limit the analysis to classical isotropic hardening. With that purpose, we replace, by means of the Chen-Mangasarian Chen and Mangasarian (1995) functions, the classical complementarity conditions by a single smooth equation. Elasto-plastic constitutive laws in Voigt form are therefore given as:

$$\mathscr{C}_{\text{linear}}^{-1}\Delta\hat{\boldsymbol{S}}_{ab} - \boldsymbol{n}\Delta\boldsymbol{\gamma} = \boldsymbol{0} \tag{46}$$

$$\mu^{\star}\Delta\boldsymbol{\gamma} - \langle \mu^{\star}\Delta\boldsymbol{\gamma} + \boldsymbol{\phi}\rangle = 0 \tag{47}$$

where, in (46), $\mathscr{C}_{\text{linear}}$ is the Hookean matrix, $\Delta\hat{\boldsymbol{S}}_{ab} = \mathscr{C}_{\text{linear}}\boldsymbol{E}_{ab} - \Delta\check{\boldsymbol{S}}_{ab}$ is the plastic stress increment, $\boldsymbol{n}$ is the matrix of flow vectors and $\Delta\boldsymbol{\gamma}$ is the matrix of plastic multiplier increments. In equation (47) $\mu^{\star}$ is a scaling parameter and $\boldsymbol{\phi}$ is the matrix of yield functions. Further details concerning this approach can be consulted in Areias, Dias-da Costa, Pires, and Infante Barbosa (2011), and in particular the determination of $\mathscr{C}$, necessary for the linearized form (28).

6 Verification tests

6.1 Patch test

Three tests based on the same geometry are performed (in-plane tension, in-plane bending and transverse shear, see Figure 4) to assess the asymmetric formulation. Nodal coordinates are the ones in the textbook by Hughes Hughes (2000). The element passes all tests.

6.2 Plane, beam and plate bending tests

Traditional tests confirming the correct implementation *in the linear case* for plane, beam and plate bending problems are shown in Figure 5 (relevant data for the tests)

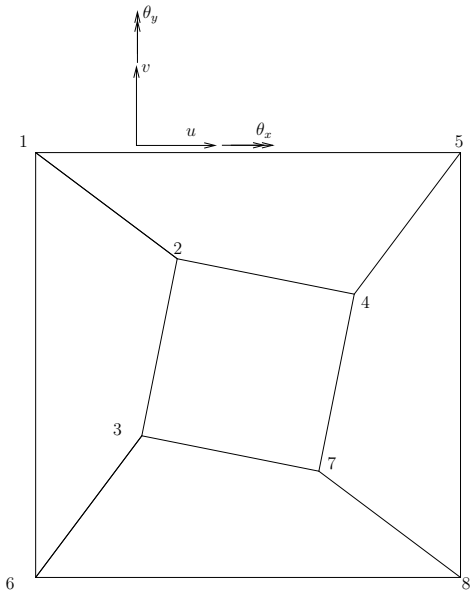

Coordinates:
1: 0.00,3.00
2: 1.00,2.25
3: 0.75,1.00
4: 2.25,2.00
5: 3.00,3.00
6: 0.00,0.00
7: 2.00,0.75
8: 3.00,0.00

Cases (linear displacement and rotation):
I - u_6=0, v_6=0, u_8=1, v_8=0, u_1=0, u_5=1
II - u_6=0, v_6=0, u_8=0, v_8=1, u_1=0, v_1=0, u_5=0, v_5=1
III - $\boldsymbol{u}_6 = \mathbf{0}$, θ_{8y}=1, $\boldsymbol{u}_1 = \mathbf{0}$, θ_{5y}=1

Figure 4: Patch test data.

and in Figures 6 and 7 (comparisons with results from the literature). Exceptionally good results are obtained, considering that only 4 enhanced metric degrees-of-freedom are used for the shell (18 were used in the 3D element of reference Areias, César de Sá, Conceição António, and Fernandes (2003)). In Figure 7 comparisons are made with the results presented in references Pian and Sumihara (1984); Bathe and Dvorkin (1986); Andelfinger and Ramm (1993); Liu, Hu, and Belytschko (1994); Piltner and Taylor (1995); Sze, Kim, and Soh (1997); Liu, Guo, and Belytschko (1998); Sansour and Bocko (1998); Areias, César de Sá, Conceição António, and Fernandes (2003) with exceptional performance.

For problem #6, Table 2 shows a comparison between the present work and the results obtained with the element of Pian and Sumihara Pian and Sumihara (1984), Simo and Armero Q1/E4 Simo and Armero (1992) and the element by Korelc and Wriggers Korelc and Wriggers (1997). Note that their element is exactly integrated and therefore unsuited for more complex problems (at the constitutive level). That being the case, our work shows the best performance in this difficult benchmark, including the Pian and Sumihara element.

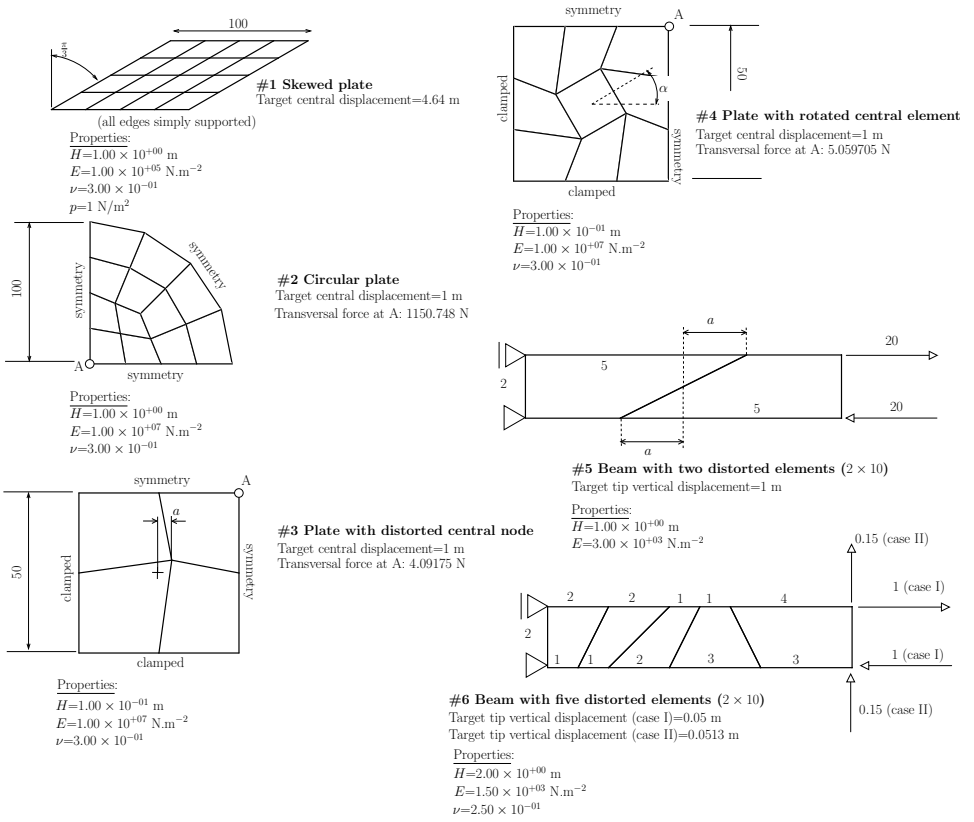

Figure 5: Linear plane, beam and plate bending tests: relevant data and target values for monitored nodes.

Table 2: Percentage of error for the beam with five distorted elements (#6).

	Error (case I)	Error (case II)
Present work	-2.70%	-3.06%
Pian and Sumihara 1984	-3.82%	-3.92%
Simo and Armero 1992	-4.00%	-4.01%
Korelc and Wriggers 1997 (exactly integrated)	-0.16%	-0.2%

6.3 Linear shell tests

Experimentation with element technology reveals that linear tests are fundamental in assessing competitiveness for both linear and nonlinear codes. The quality of the results in many nonlinear problems is conditioned by the corresponding lin-

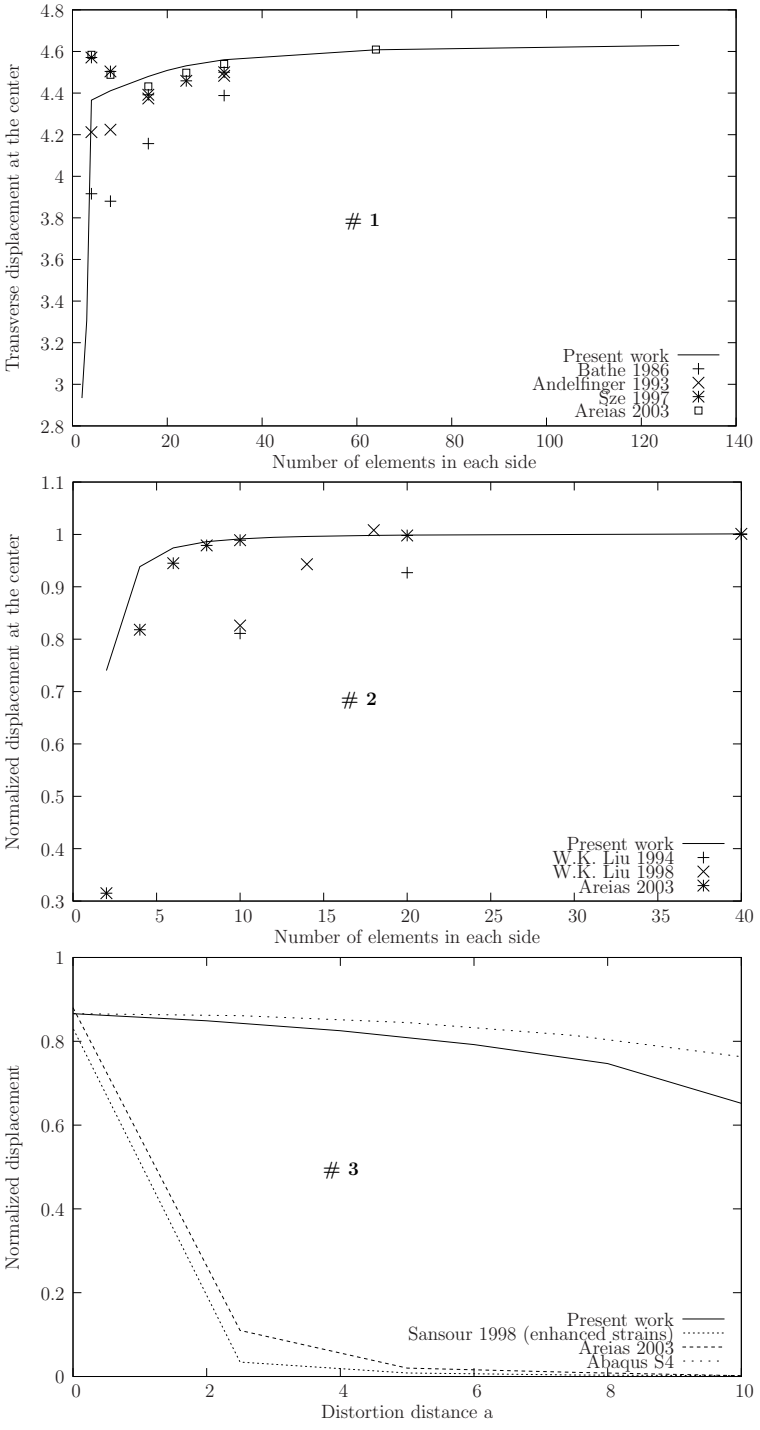

Figure 6: Verification tests: linear plane problems, comparison with alternative formulations (problems #1, #2 and #3).

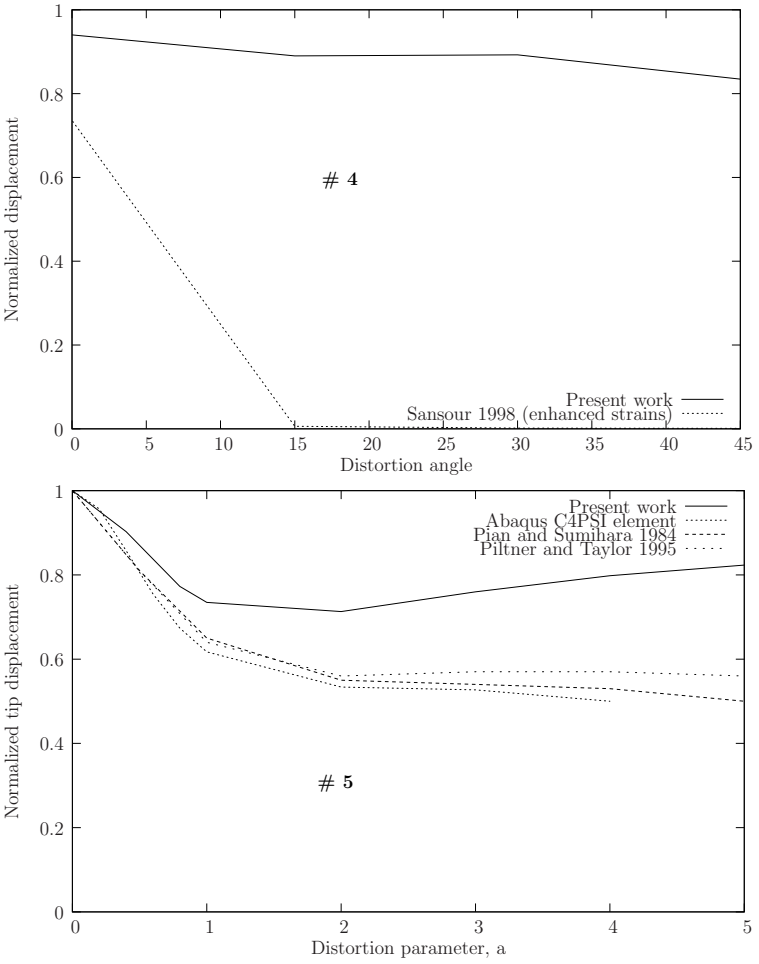

Figure 7: Verification tests: linear plane problems, comparison with alternative formulations (problems #4 and #5).

ear performance. However, due to the presence of interfering constitutive laws, updated vs. total Lagrangian approaches, stress integration and other interfering factors, results in nonlinear problems are seldom conclusive concerning the actual accuracy of the underlying interpolation technique. Therefore, we first focus on linear shell problems. Five classical shell tests are performed as Figure 8 depicts. The Figure contains all relevant data to reproduce the problems. Present results are compared with well known high performance elements in Figures 9 and 10. Test #1 is the well-known pinched cylinder problem where a reference value of

1.82488×10^{-5} m is used in the normalization, in agreement with Simo, Fox and Rifai Simo, Fox, and Rifai (1989). Results shown in Figure 9 attest the excellent performance of the present element. Test #2 is the Scordelis-Lo roof (see MacNeal and Harder (1985)) in which our element was found to have similar performance to the S4 element from Abaqus. Test #3 is the closed pinched hemisphere[8] with a target value of the radial displacement of 0.0924 Simo, Fox, and Rifai (1989). In this test, we found that our element converges faster than the S4 element for coarse meshes. The test #4 is the so-called twisted beam and it has been adopted in many references with several variants. Our variant is the most demanding (with a thickness of 0.0032 m) and was proposed by Belytschko and Wong Belytschko and Wong (1989). Two load cases are inspected, as indicated in Figure 8. Excellent results were obtained by the present formulation in case A. Test #5 is the so-called Raasch's hook (cf. Schoop, Hornig, and Wenzel (2002)) and involves bending and torsion. The target value adopted here is 5.02 consistent units (also employed in the first Author's Ph.D. thesis and Abaqus/Standard benchmark suite). Results appear somehow worse than Abaqus S4 but the target value is well approximated by the present element. An inspection shows very good results for coarse meshes. The present results are better than the previous high-performance element HIS (cf. Areias, César de Sá, Conceição António, and Fernandes (2003)) and QBM (cf. Areias, Song, and Belytschko (2005)). Overall, the present work shows one of the best performing elements four-node shell elements.

6.4 Nonlinear problems

The purpose of this section is to show the applicability to nonlinear problems and the *unprecedented* robustness of the solutions, specifically:

- Higher levels or load and displacement than published results.
- Very large load steps and consistency of results between different load steps (when considering hyperelasticity or metal elasto-plasticity)
- Asymptotically quadratic rate of convergence.

Nonlinear problems are shown in two sets: finite-displacement elastic problems (hypoelastic) and finite strain plasticity problems. More complex constitutive laws can of course be used (the reader can consult Areias, Dias-da Costa, Pires, and Infante Barbosa (2011) for an efficient semi-implicit implementation of anisotropic plasticity) but this is not the theme of this work. In addition, thickness variation was treated in another work (see Areias, Ritto-Corrêa, and Martins (2010)) and is not dealt in here.

[8] The open 18° variant is now known to be redundant.

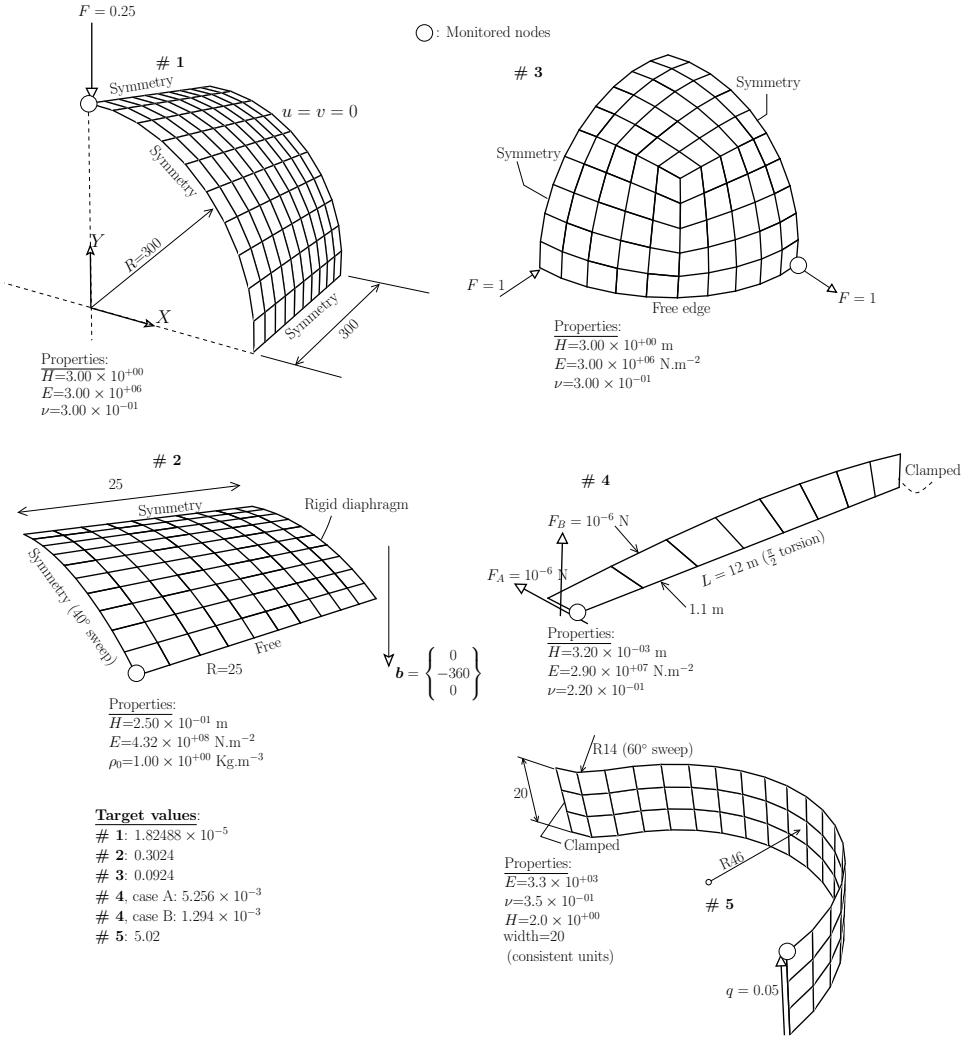

Figure 8: Linear shell tests: relevant data and target values for monitored nodes.

Four classical geometrically non-linear problems are solved, with the corresponding data summarized in Figure 11. Results shown in figures 12, 13 and 14 attest the exceptional robustness of the proposed formulation. Newton-Raphson convergence is asymptotically quadratic (Figure 13) since an exact linearization is performed.

Two classical finite strain plasticity problems are solved, using our recent algorithm (cf. Areias, Dias-da Costa, Pires, and Infante Barbosa (2011)): the elasto-plastic plate under deformation-dependent pressure and the pinched cylinder (both with

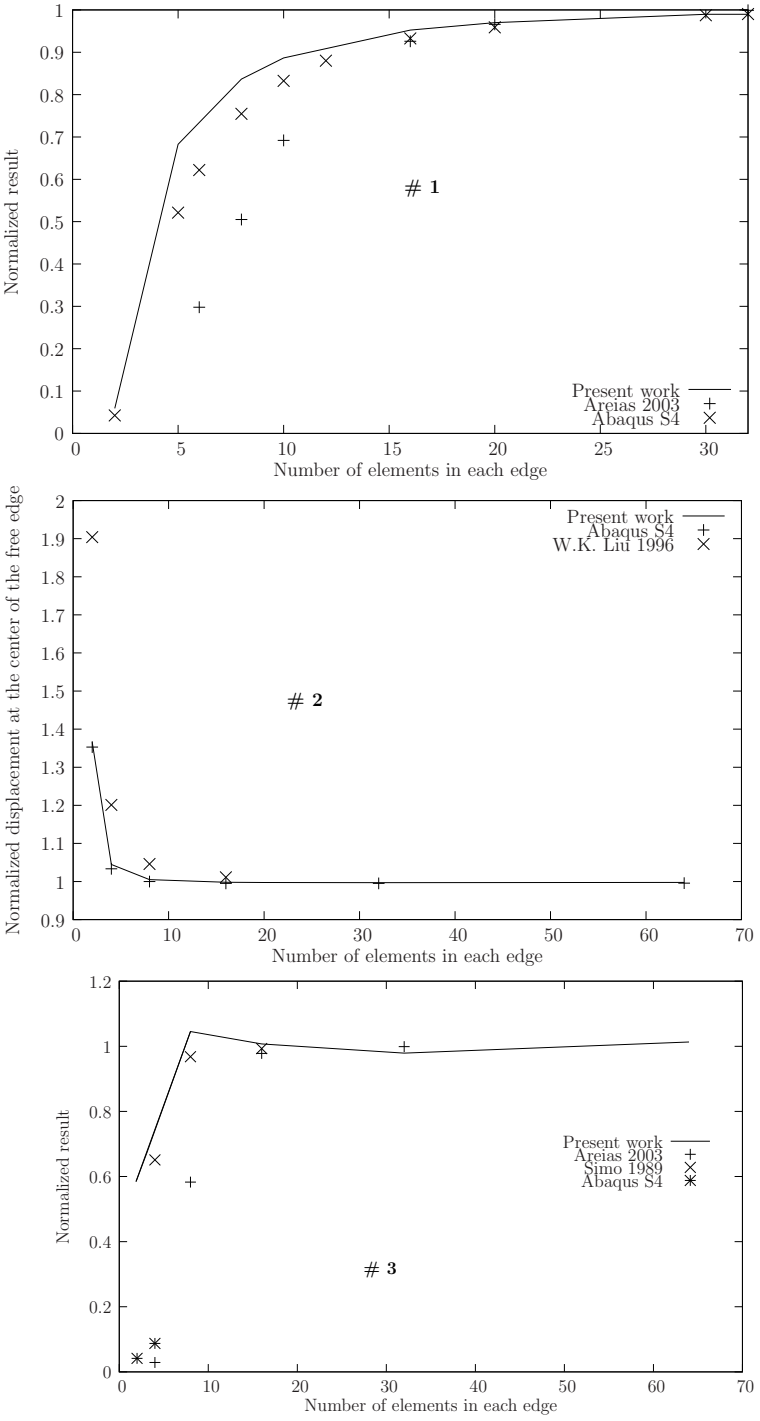

Figure 9: Linear shell tests: results for problems #1 to #3.

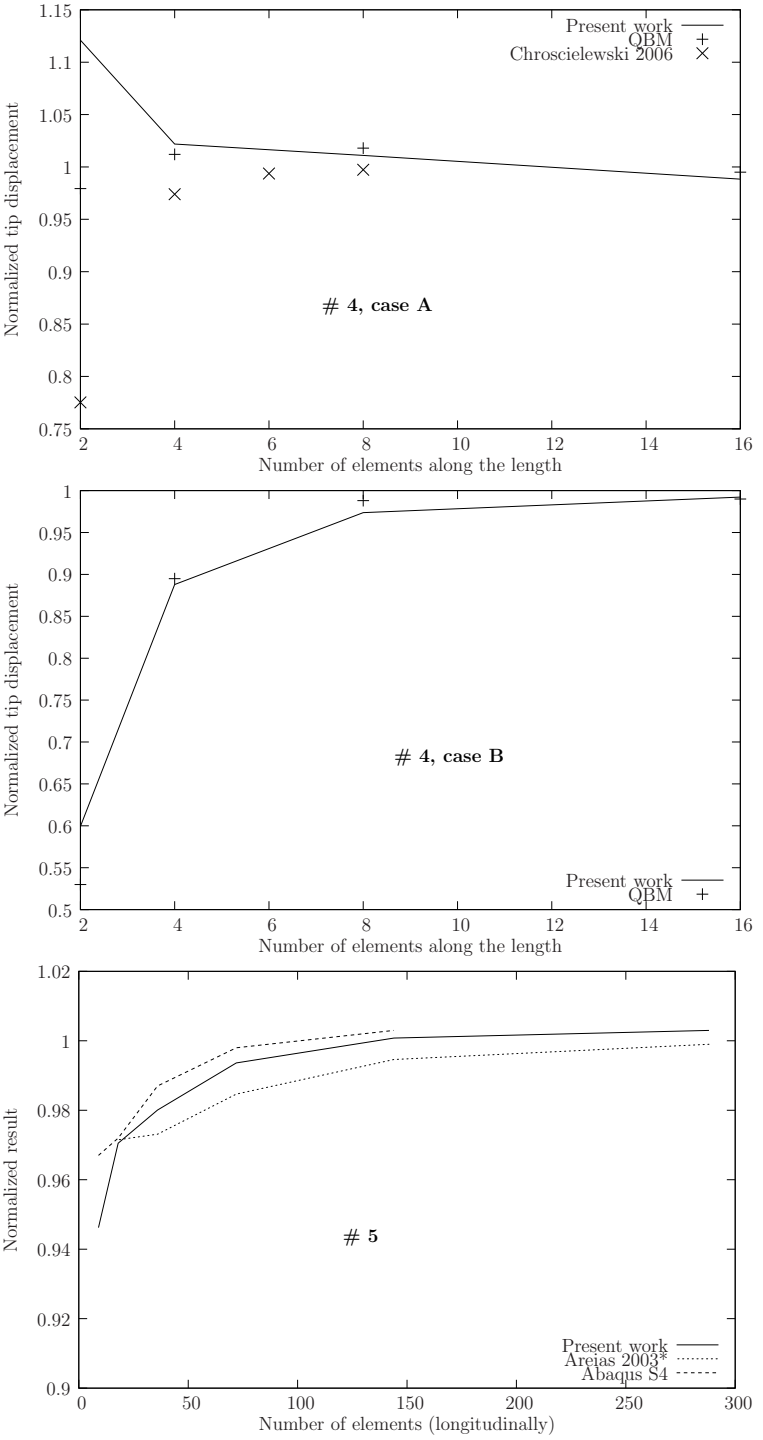

Figure 10: Linear shell tests: results for problems #4 and #5.

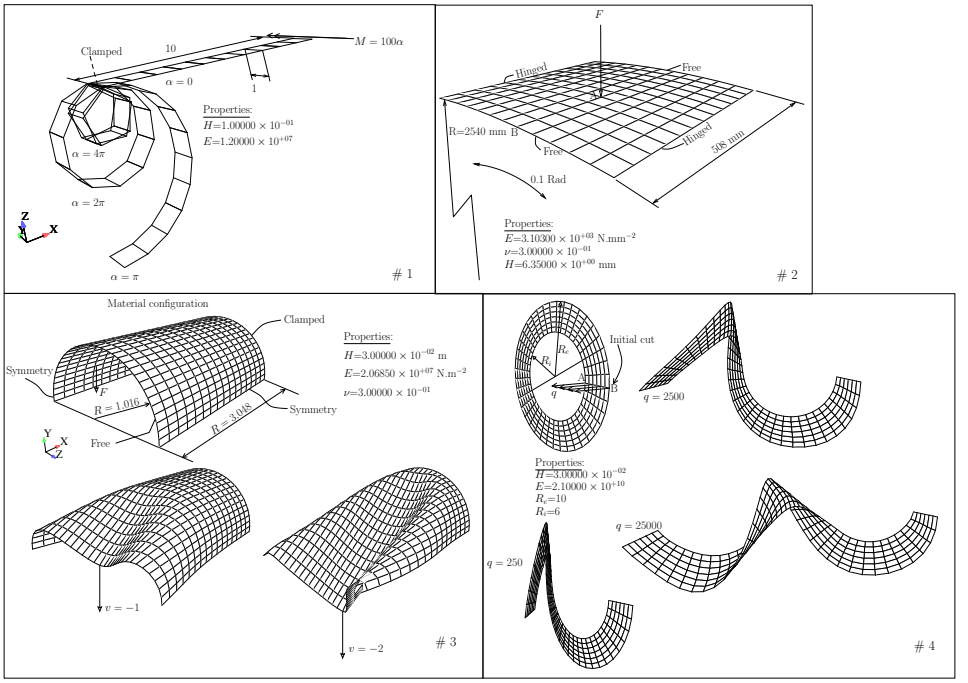

Figure 11: Finite-displacement problems: relevant data and target values for monitored nodes.

plane stress von-Mises plasticity). Relevant data and deformed meshes (and contour plots) related to these problems are shown in Figure 16. The plate under pressure was described by Hauptmann *et al.* Hauptmann, Doll, Harnau, and Schweizerhof (2001) and further detailed in Areias, César de Sá, Conceição António, and Fernandes (2003). It consists of a plate with dimensions $508 \times 508 \times 2.54$ consistent units. Elasticity modulus is $E = 6.9 \times 10^4$ consistent units, Poisson coefficient $\nu = 0.3$ and the yield stress is $\sigma_y = 248$ consistent units. One-fourth of the plate is analyzed with 32×32 elements with a sequence of deformed meshes and the effective plastic strain contour plot shown in Sub-Figure 15(a). Results presented in Figure 16 show slightly less stiff results than the ones in Areias, César de Sá, Conceição António, and Fernandes (2003) and a remarkable time-step size insensitivity (both 10 and 100 steps produce nearly the same results), further attesting the robustness of the consistent updated-Lagrangian algorithm. The pinched cylinder test with the same boundary conditions as in Figure is depicted in Sub-Figure 15(b) was also tested in Areias, César de Sá, Conceição António, and Fernandes (2003). It consists of a cylinder with 300 mm of radius, with $E = 3000$ MPa, $\nu = 0.3$ and

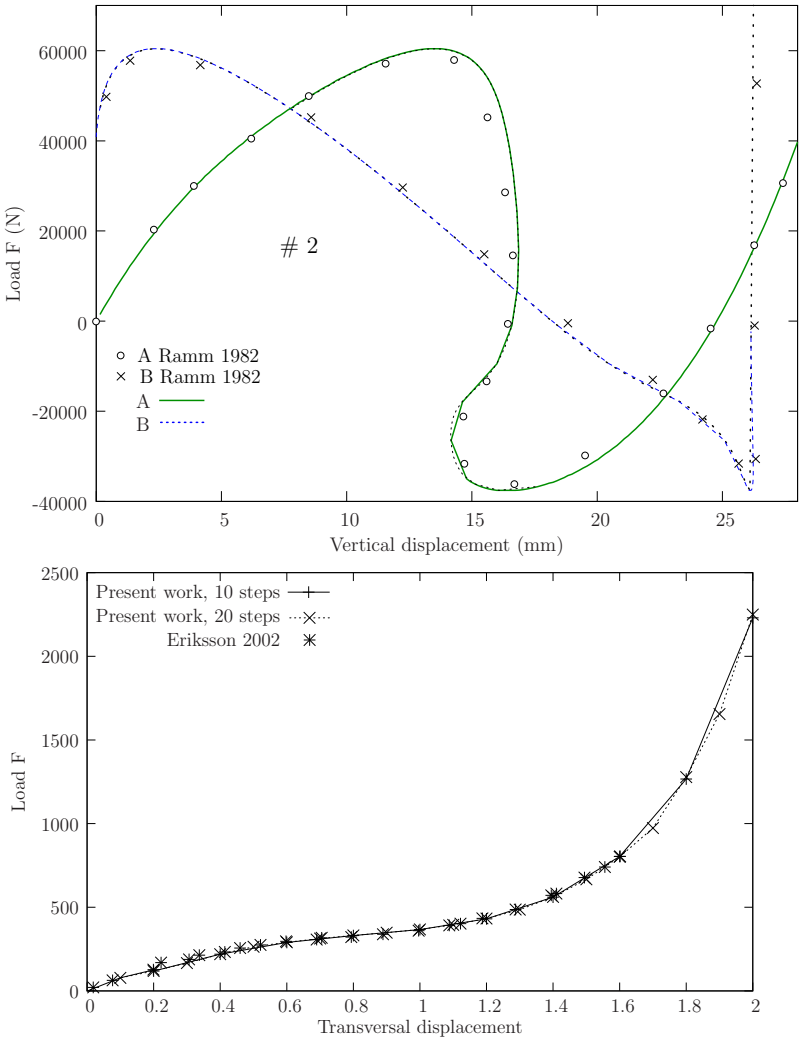

Figure 12: Finite-displacement problems: specific results compared with reference numerical solutions Ramm (1982) and Eriksson and Pacoste (2002).

a linear hardening law: $\sigma_y = 24.3 + 300\varepsilon_p$ MPa. Load-deflection results for the 16×16 are shown in Figure, a little stiffer than the ones by Wagner, Klinkel and Gruttmann Wagner, Klinkel, and Gruttmann (2002) for high values of displacement.

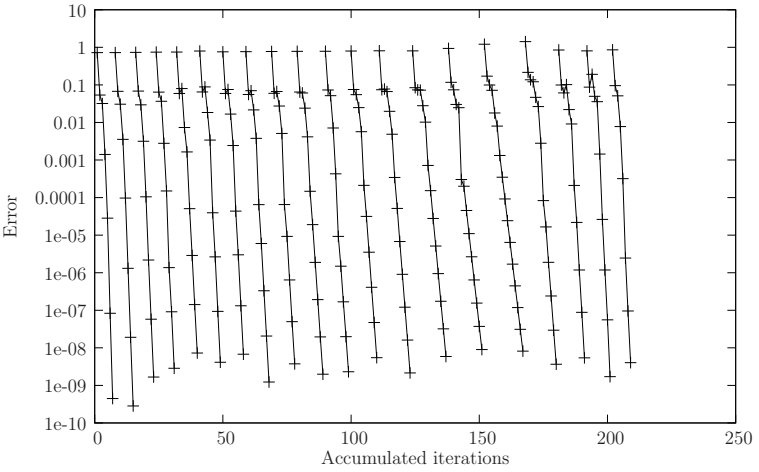

Figure 13: Error values vs. iterations for the 20 step case (clamped cylinder).

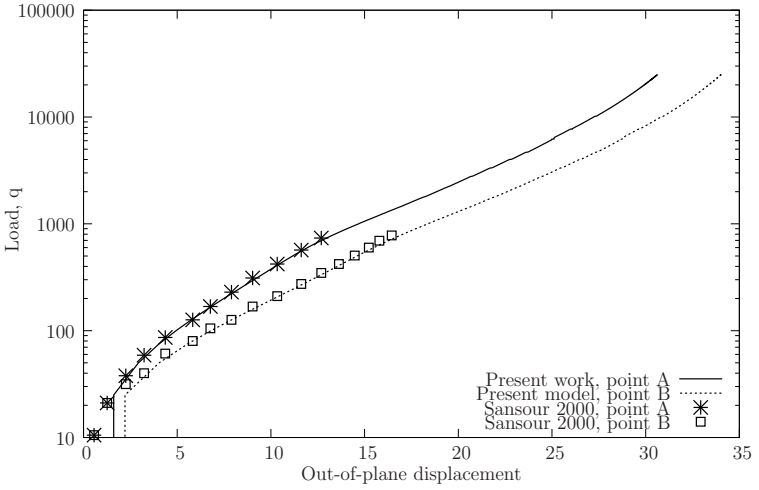

Figure 14: Ring test (#4): comparison with the results of Sansour and Bocko Sansour and Kollmann (2000).

7 Conclusions

We presented a non-symmetric Petrov-Galerkin using cartesian coordinates for the trial functions to obtain a quadrilateral shell element with high coarse-mesh accuracy and robustness. The element contains assumed metric components and incompatible modes in the test functions and incompatible modes in the trial func-

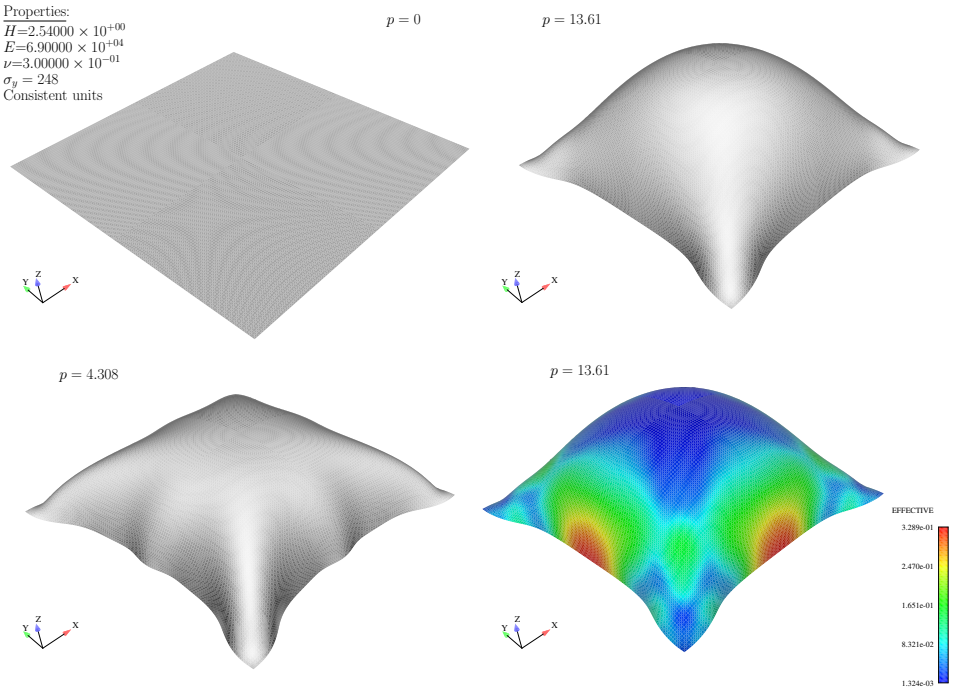

(a) Square plate under deformation-dependent pressure: data and sequence of deformed meshes. Edge displacements are prescribed in the out-of-plane direction.

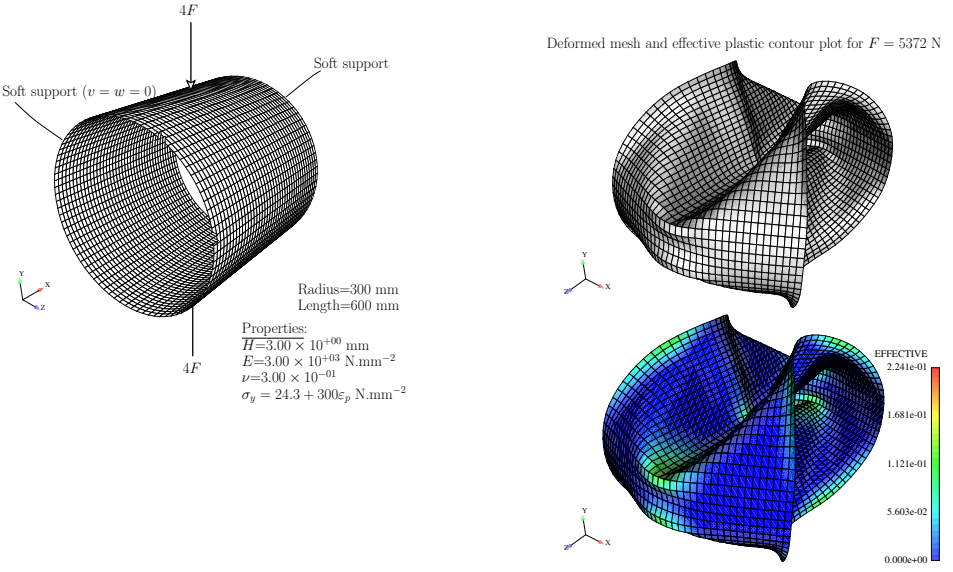

(b) Pinched cylinder: relevant data, deformed mesh and effective plastic strain contour plot.

Figure 15: Finite strain plasticity problems: relevant data and results.

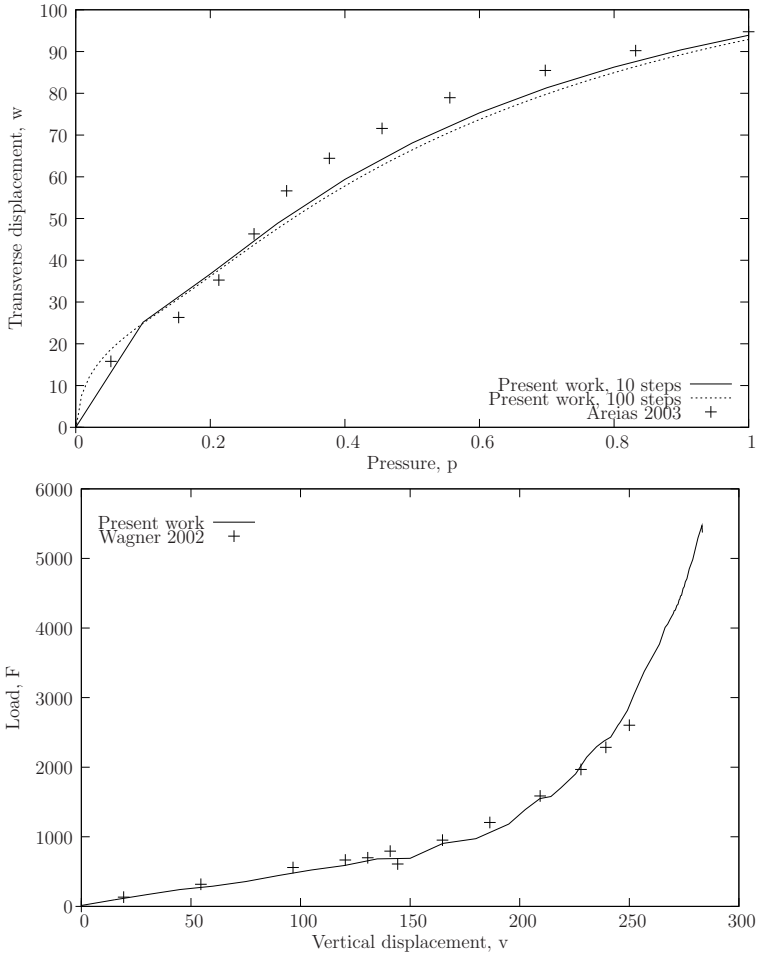

Figure 16: Finite strain plasticity problems: load/deflection results compared with Areias, César de Sá, Conceição António, and Fernandes (2003) and Wagner, Klinkel, and Gruttmann (2002).

tions. These are derived directly in Cartesian coordinates for a (moving) reference configuration. A consistent updated-Lagrangian algorithm was proposed with exact linearization which provided a very simple connection with the constitutive algorithms previously developed. The algorithm is both equilibrium-consistent and consistently linearized. With that purpose, a simplification of our recent multiple-surface algorithm Areias, Dias-da Costa, Pires, and Infante Barbosa (2011) was employed with a high degree of success and excellent time-step independence. The

Patch test is passed in its three variations. Linear examples showed remarkable robustness and mesh distortion insensitivity. The distortion tests results are better than with the Pian-Sumihara element. Several geometrically nonlinear problems were tested with very good robustness and accuracy, a fact that we attribute to the form of the trial functions. The use of a correct transport stress seems to solve the well known dependence observed in inconsistent updated-Lagrangian algorithms. Two classical finite strain elasto-plastic problems are also shown, which complete the assessment of the new element. Further exploration of the element and more applications are being carried out, including applications to fracture. Finally, we must remark that the linearization was partly performed with Wolfram Mathematica Research Inc (2007) with the AceGen Korelc (2002) add-on. The software employed was SIMPLAS Areias.

Acknowledgement: The authors gratefully acknowledge financing from the "Fundação para a Ciência e a Tecnologia" under the Project PTDC/EME-PME/108751 and the Program COMPETE FCOMP-01-0124-FEDER-010267. The corresponding author would like to thank Professor J. Infante Barbosa for a preliminary discussion of this manuscript.

References

Andelfinger, U.; Ramm, E. (1993): EAS-elements for two-dimensional, three-dimensional, plate and shell structures and their equivalence to HR-elements. *Int J Numer Meth Eng*, vol. 36, pp. 1311–1337.

Antman, S. (2005): *Nonlinear problems of elasticity*. Springer, Second edition.

Antman, S.; Marlow, R. (1991): Material constraints, lagrange multipliers, and compatibility. *Arch Ration Mech An*, vol. 116, pp. 257–299.

Areias (): Simplas. https://ssm7.ae.uiuc.edu:80/simplas.

Areias, P.; Belytschko, T. (2006): Analysis of finite strain anisotropic elastoplastic fracture in thin plates and shells. *J Aerospace Eng*, vol. 19, no. 4, pp. 259–270.

Areias, P.; César de Sá, J.; Conceição António, C.; Fernandes, A. (2003): Analysis of 3D problems using a new enhanced strain hexahedral element. *Int J Numer Meth Eng*, vol. 58, pp. 1637–1682.

Areias, P.; Dias-da Costa, D.; Pires, E.; Infante Barbosa, J. (2011): A new semi-implicit formulation for multiple-surface multiplicative plasticity. *Comput Mech*. In press.

Areias, P.; Garção, J.; Pires, E.; Infante Barbosa, J. (2011): Exact corotational shell for finite strains and fracture. *Comput Mech*, vol. 48, pp. 385–406.

Areias, P.; Rabczuk, T. (2010): Smooth finite strain plasticity with nonlocal pressure support. *Int J Numer Meth Eng*, vol. 81, pp. 106–134.

Areias, P.; Ritto-Corrêa, M.; Martins, J. (2010): Finite strain plasticity, the stress condition and a complete shell model. *Comput Mech*, vol. 45, pp. 189–209.

Areias, P.; Song, J.-H.; Belytschko, T. (2005): A finite-strain quadrilateral shell element based on discrete kirchhoff-love constraints. *Int J Numer Meth Eng*, vol. 64, pp. 1166–1206.

Bathe, K.-J.; Dvorkin, E. (1986): A formulation of general shell elements-the use of mixed interpolation of tensorial components. *Int J Numer Meth Eng*, vol. 22, pp. 697–722.

Belytschko, T.; Liu, W.; Moran, B. (2000): *Nonlinear finite elements for continua and structures*. John Wiley & Sons.

Belytschko, T.; Wong, B. (1989): Assumed strain stabilization procedure for the 9-node Lagrance shell element. *Int J Numer Meth Eng*, vol. 28, pp. 385–414.

Brank, B.; Ibrahimbegovic, A. (2001): On the relation between different parametrizations of finite rotations for shells. *Eng Computation*, vol. 18, pp. 950–973.

Bruhns, O.; Meyers, A.; Xiao, H. (2004): On non-corotational rates of oldroyd's type and relevant issues in rate constitutive formulations. *P Roy Soc Lond A Mat*, vol. 460, pp. 909–928.

Chen, C.; Mangasarian, O. (1995): Smoothing methods for convex inequalities and linear complementarity problems. *Math Program*, vol. 71, no. 1, pp. 51–69.

Crisfield, M.; Peng, X. (1996): Instabilities induced by coarse meshes for a nonlinear shell problem. *Eng Computation*, vol. 13, no. 6, pp. 110–114.

Dvorkin, E.; Bathe, K. (1984): A continuum mechanics based four node shell element for general nonlinear analysis. *Eng Computation*, vol. 1, pp. 77–88.

Eriksson, A.; Pacoste, C. (2002): Element formulation and numerical techniques for stability problems in shells. *Comp Method Appl M*, vol. 191, pp. 3775–3810.

Hauptmann, R.; Doll, S.; Harnau, M.; Schweizerhof, K. (2001): Solid-shell elements with linear and quadratic shape functions at large deformations with near incompressible materials. *Comput Struct*, vol. 79, pp. 1671–1685.

Holzapfel, G. (2000): *Nonlinear solid mechanics: a continuum approach for engineers*. John Wiley and Sons.

Hughes, T. (2000): *The finite element method*. Dover Publications. Reprint of Prentice-Hall edition, 1987.

Hughes, T.; Liu, W. (1981): Nonlinear finite element analysis of shells: Part I: Three-dimensional shells. *Comp Method Appl M*, vol. 26, pp. 331–362.

Korelc, J. (2002): Multi-language and multi-environment generation of nonlinear finite element codes. vol. 18, no. 4, pp. 312–327.

Korelc, J.; Wriggers, P. (1997): Improved enhanced strain four-node element with Taylor expansion of the shape functions. *Int J Numer Meth Eng*, vol. 40, pp. 407–421.

Liu, W.; Guo, Y.; Belytschko, T. (1998): A multiple-quadrature eight-node hexahedral finite element for large deformation elastoplastic analysis. *Comp Method Appl M*, vol. 154, pp. 69–132.

Liu, W.; Hu, Y.-K.; Belytschko, T. (1994): Multiple quadrature underintegrated finite elements. *Int J Numer Meth Eng*, vol. 37, pp. 3263–3289.

MacNeal, R.; Harder, R. (1985): A proposed standard set of problems to test finite element accuracy. *Finite Elem Anal Des*, vol. 1, pp. 1–20.

Ogden, R. (1997): *Non-linear elastic deformations*. Dover Publications, Mineola, New York.

Ooi, E.; Rajendran, S.; Yeo, J. (2004): A 20-node hexahedron element with enhanced distortion tolerance. *Int J Numer Meth Eng*, vol. 60, pp. 2501–2530.

Park, K.; Stanley, G. (1986): A curved C0 shell element based on assumed natural-coordinate strains. *J Appl Mech-ASME*, vol. 53, pp. 278–290.

Pian, T.; Sumihara, K. (1984): Rational approach for assumed stress finite elements. *Int J Numer Meth Eng*, vol. 20, pp. 1685–1695.

Piltner, R.; Taylor, R. (1995): A quadrilateral mixed finite element with two enhanced strain modes. *Int J Numer Meth Eng*, vol. 38, pp. 1783–1808.

Rabczuk, T.; Areias, P. (2006): A meshfree thin shell for arbitrary evolving cracks based on an external enrichment. *Comput Model Eng Sci*, vol. 16, no. 2, pp. 115–130.

Rabczuk, T.; Areias, P.; Belytschko, T. (2007): A meshfree thin shell method for non-linear dynamic fracture. *Int J Numer Meth Eng*, vol. 72, pp. 524–548.

Rajendran, S.; Liew, K. (2003): A novel unsymmetric 8-node plane element immune to mesh distortion under a quadratic field. *Int J Numer Meth Eng*, vol. 58, pp. 1718–1748.

Ramm, E. (1982): The Riks/Wempner approach - an extension of the displacement control method in nonlinear analyses. In *Recent advances in non-linear computational mechanics*, chapter 3, pp. 63–86. Pineridge Press Limited, Swansea, U.K.

Research Inc, W. (2007): Mathematica, 2007.

Sansour, C.; Bocko, J. (1998): On hybrid stress, hybrid strain and enhanced strain finite element formulations for a geometrically exact shell theory with drilling degrees of freedom. *Int J Numer Meth Eng*, vol. 43, no. 1, pp. 175–192.

Sansour, C.; Kollmann, F. (2000): Families of 4-node and 9-node finite elements for a finite deformation shell theory. an assessment of hybrid stress, hybrid strain and enhanced strain elements. *Comput Mech*, vol. 24, pp. 435–447.

Schoop, H.; Hornig, J.; Wenzel, T. (2002): Remarks on Raasch's hook. *Tech Mech*, vol. 4, no. 22, pp. 259–270.

Simo, J. (1992): Algorithms for static and dynamic multiplicative plasticity that preserve the classical return mapping schemes of the infinitesimal theory. *Comp Method Appl M*, vol. 99, pp. 61–112.

Simo, J.; Armero, F. (1992): Geometrically non-linear enhanced strain mixed methods and the method of incompatible modes. *Int J Numer Meth Eng*, vol. 33, pp. 1413–1449.

Simo, J.; Fox, D.; Rifai, M. (1989): Geometrically exact stress resultant shell models: Formulation and computational aspects of the nonlinear theory. In Noor, A.; Belytschko, T.; Simo, J.(Eds): *Analytical and Computational Models of Shells*, volume 3 of *CED*, pp. 161–190, San Francisco, CA. ASME, ASME.

Simo, J.; Hughes, T. (2000): *Computational Inelasticity*. Springer, Corrected Second Printing edition.

Sze, K.; Kim, Y.; Soh, A. (1997): A hybrid stress quadrilateral shell element with full rotational DOFS. *Int J Numer Meth Eng*, vol. 40, pp. 1785–1800.

Truesdell, C.; Noll, W. (2004): *The non-linear field theories of mechanics*. Springer, Third edition.

Wagner, W.; Klinkel, S.; Gruttmann, F. (2002): Elastic and plastic analysis of thin-walled structures using improved hexahedral elements. *Comput Struct*, vol. 80, pp. 857–869.

Wilson, E.; Taylor, R.; Doherty, W.; Ghaboussi, J. (1973): Incompatible displacement models. In Fenves, S.; Perrone, N.; Robinson, A.; Schnobrich, W.(Eds): *Numerical and Computer Models in Structural Mechanics*, pp. 43–57. Academic Press, New York.

Wriggers, P. (2008): *Nonlinear finite element methods*. Springer.